Journal of Volcanology and Geothermal Research 298 (2015) 71–84

Contents lists available at ScienceDirect

Journal of Volcanology and Geothermal Research

journal homepage: www.elsevier.com/locate/jvolgeores

Magma fracturing and degassing associated with obsidian formation: The explosive–effusive transition

Agustín Cabrera [a], Roberto F. Weinberg [a,*], Heather M.N. Wright [a,1]

[a] School of Geosciences, Monash University, Australia

ARTICLE INFO

Article history:
Received 16 December 2013
Accepted 9 July 2014
Available online 7 January 2015

Keywords:
Rhyolite
Melt fracturing
Degassing
Explosive–effusive transition
Obsidian

ABSTRACT

This paper explores the role of melt fracturing in degassing rhyolitic volcanic systems. The Monte Pilato-Rocche Rosse eruptions in Italy evolved from explosive to effusive in style, and H_2O content in quenched glasses changed over time from relatively H_2O-rich (~0.90 wt.%) to H_2O-poor dense obsidian (~0.10–0.20 wt.%). In addition, healed fractures have been recorded in all different eruptive materials, from the glass of early-erupted tube pumice and rinds of breadcrusted obsidian pyroclasts, to the glass of late-erupted dense obsidian pyroclasts, and throughout the final effusive Rocche Rosse lava flow. These rocks show multiple fault sets, some with crenulated fault planes indicating resumption of viscous flow after faulting, complex obsidian breccias with evidence for post-brecciation folding and stretching, and centimetre- to metre-thick tuffisite preserved in pyroclasts and lava, representing collapsed foam due to fracturing of vesicle walls. These microstructural observations indicate that multiple fracturing and healing events occurred during both explosive and effusive eruptions. H_2O content in glass decreases by as much as 0.14 wt.% towards healed fractures/faults and decreases in stretched obsidian breccias towards regions of intense brecciation. A drop in pressure and/or increase in temperature along fractures caused diffusive H_2O migration through melt towards fracture surfaces. Repetitive and pervasive fracturing and healing thereby create conditions for diffusive H_2O loss into fractures and subsequent escape through permeable paths. This type of progressive magma degassing provides a potential mechanism to explain the formation of dense obsidian and the evolution from explosive to effusive eruption style.

1. Introduction

Deposits from rhyolite volcanoes worldwide indicate that many eruptions evolve from explosive to effusive (e.g., Eichelberger and Westrich, 1981; Cortese et al., 1986; Dellino and La Volpe, 1995; Barclay et al., 1996; Lara, 2009; Watt et al., 2013). Recent observations of rhyolite eruptions at El Chaitén, and Puyehue–Cordón Caulle, Chile, follow the explosive–effusive pattern for rhyolite volcanoes, where Plinian explosive activity transitioned to lava effusion within a week (Castro and Dingwell, 2009; Castro et al., 2012b; Schipper et al., 2013).

The whole-rock major element composition of rhyolites extruded during explosive–effusive rhyolite eruptions is generally constant within the eruptive cycle (e.g., Gioncada et al., 2003; Pallister et al., 2013; Watt et al., 2013). Although there can be a relative increase in crystal content in the products of effusive compared to explosive eruptions (cf. Castro and Dingwell, 2009; Watt et al., 2013), commonly the main change is a decrease in volatile contents (H_2O, CO_2, F, Cl, Li, Be and S) that is recorded in matrix glasses (Newman et al., 1988; Westrich et al., 1988; Dunbar and Kyle, 1992; Barclay et al., 1996; Lowenstern et al., 2012).

H_2O is the dominant volatile phase in volcanic melts, and dissolved H_2O contents in erupted rhyolite glasses vary from ~2.2 wt.% in explosive products, to between 0.5 and 0.1 wt.% in effusive deposits (e.g., Eichelberger and Westrich, 1981; Westrich et al., 1988; Castro and Dingwell, 2009). Generally, the juvenile components of explosive rhyolite deposits are dominantly pumice, whereas obsidian (vesicle-poor glass) forms a small proportion of the deposits (e.g., Eichelberger and Westrich, 1981; Schipper et al., 2013). However, H_2O-poor obsidian dominates amongst effusive deposits (Fink, 1980; Manley and Fink, 1987; Stevenson et al., 1994; Tuffen and Castro, 2009; Furukawa et al., 2010). Primary magmatic H_2O dissolved in glass from pyroclastic obsidian and feeder dikes can vary widely from 2.2 wt.% down to values in equilibrium with atmospheric pressure (0.10 wt.%; e.g., Eichelberger and Westrich, 1981; Westrich et al., 1988; Castro and Dingwell, 2009; Watkins et al., 2012). In contrast, glasses from obsidian lava record a narrower range at low values (0.1–0.5 wt.%; Westrich et al., 1988; Castro et al., 2005; Clay et al., 2012; von Aulock et al., 2013).

DOI of original article: http://dx.doi.org/10.1016/j.jvolgeores.2014.07.004.
* Corresponding author at: School of Geosciences, Building 28, Monash University, Clayton, VIC 3800, Australia.
E-mail address: Roberto.Weinberg@monash.edu (R.F. Weinberg).
[1] Currently at: Cascades Volcano Observatory, USGS, 1300 SE Cardinal Court, Building 10, Suite 100, Vancouver, WA 98683, USA.

http://dx.doi.org/10.1016/j.jvolgeores.2014.12.014
0377-0273/

The explosivity and style of volcanic eruptions are controlled by the ability of magmatic gas to escape as magma ascends and decompresses. Magma overpressure driving eruption is a function of the balance between gas exsolution and gas loss (e.g., Sparks, 2003). Permeable networks of connected bubbles and shear-induced brittle fractures are thought to allow gas migration and outgassing of the system (Eichelberger et al., 1986; Jaupart and Allègre, 1991; Stasiuk et al., 1996; Gonnermann and Manga, 2003; Cabrera et al., 2011; Holland et al., 2011; Lavallée et al., 2013; Schipper et al., 2013). The critical vesicularity at which significant gas loss occurs varies due to complex relationships between porosity and permeability (Rust and Cashman, 2004), partly controlled by shear flow (Wright and Weinberg, 2009). Measurements of the permeability of natural, vesicular volcanic samples and laboratory analogs indicate that bubbles form a percolating network at porosities between 30 and 80 vol.%, depending on melt viscosity, crystallinity, magnitude of shear, and bubble expansion rate (e.g., Klug and Cashman, 1996; Saar and Manga, 1999; Mueller et al., 2005).

For the expected range of permeabilities in vesicular magmas (10^{-15} to 10^{-12} m^2; cf. Rust and Cashman, 2011), calculated degassing times are longer than the estimated timescale of magma ascent through shallow conduits (Gonnermann and Manga, 2003; Takeuchi et al., 2008; Okumura et al., 2009). Slow degassing implies that another mechanism must explain the gas loss required to defuse explosive volcanic systems and give rise to effusive lava flows. Shearing experiments and measurements of natural vesicular rhyolite samples indicate that deformation of foams can greatly enhance sample permeability (Okumura et al., 2009; Wright and Weinberg, 2009; Okumura et al., 2010; Caricchi et al., 2011) and give rise to oriented, tube-like, bubble–bubble open paths, thought more typical of the relatively deep parts of conduit based on their presence in highly vesicular pumiceous pyroclasts (Blower, 2001; Wright et al., 2006; Okumura et al., 2009).

Torsional shear deformation experiments on vesicular samples have also shown that foams can sustain brittle fracture and degas (Okumura et al., 2010). However, these experiments also indicate that slip in the fractured interface prevents further brittle failure and shear-induced bubble coalescence. Healing of fractures results in resumption of viscous deformation (Tuffen et al., 2003), thus fracturing will only be a significant degassing mechanism if magma fracturing and healing events are common and pervasive (Okumura et al., 2010).

Different mechanisms have been proposed to explain the lack of preserved open permeable pathways in obsidian and the change from explosive to effusive behaviour in silicic volcanic systems. Vesicle collapse as well as fracturing and healing of melt, both induced by magma shearing in the conduit, can potentially explain: a) degassing, b) low porosity in eruptive products, and c) change in eruptive behaviour from explosive to effusive (Eichelberger et al., 1986; Gonnermann and Manga, 2003; Castro et al., 2012a; Okumura et al., 2013; Schipper et al., 2013). Cabrera et al. (2011) measured H_2O content across a healed fault in pyroclastic obsidian glass and demonstrated that fractures are directly related to degassing by providing low pressure and/or high temperature sites, which lead to diffusion of volatiles from the melt into the fracture, and provide a permeable path for gas escape.

In order to account for considerable degassing of melt and explain explosive to effusive transitions, fracturing and healing must be a pervasive and repetitive process (e.g., Gonnermann and Manga, 2003; Rust and Cashman, 2007; Cabrera et al., 2011; Castro et al., 2012b). Repeated fracturing and healing of melt during eruptions have been demonstrated in several volcanoes, both in the conduit during ascent and in lavas (Stasiuk et al., 1996; Tuffen et al., 2003; Rust et al., 2004; Tuffen and Dingwell, 2005; Rust and Cashman, 2007; Tuffen and Castro, 2009; Tuffen et al., 2010; Castro et al., 2012b; Schipper et al., 2013). Estimated fracturing and healing times of obsidian glass are compatible with the time between earthquakes recorded during silicic lava eruptions (e.g., Tuffen et al., 2003; Yoshimura and Nakamura, 2010; Cabrera et al., 2011; Castro et al., 2012b).

Castro et al. (2012b) estimated the degree of melt fracture pervasiveness required to defuse El Chaitén's 2008 explosive eruption via diffusive water loss into fractures. They measured H_2O concentration profiles in the matrix glass of pyroclasts (with evidence of pervasive fracture and healing) and lava. They found that H_2O contents drop towards tuffisite veins and towards the edges of clasts within tuffisite veins. Modelled diffusion times that would account for these H_2O drops are ~10^2–10^5 s, similar to modelled times for diffusion of H_2O into healed faults in the rind of breadcrusted obsidian bombs on Lipari Island (Cabrera et al., 2011). The transition from explosive to effusive behaviour occurred within 10 days, therefore Castro et al. (2012b) argued that unless the magma at El Chaitén was fragmented into mm-size particles across the conduit, shear-induced fragmentation could only have accounted for enhanced degassing from magma near the conduit margins. However, the hybrid and concomitant explosive–effusive phases at Chaitén and Cordón Caulle rhyolite eruptions in Chile, indicate the occurrence of shear-induced degassing processes at the scale of the conduit (Schipper et al., 2013). Schipper et al. (2013) proposed that during the Cordón Caulle eruptions, areas of strain localisation and shear-induced magma-fragmentation were not restricted to conduit margins, but rather prevailed within the conduit through a network of branched shallow permeable zones that extended over more than 100 m depth and intersected highly sheared vesicular melt. These zones allowed degassing, where permeable gas escape from a foamed magma dominated over diffusive gas escape into fractures (Schipper et al., 2013). In this paper, we investigate the extent of fracturing and healing in eruptive products; the resultant effects on H_2O content of melt; and infer relationships between fracture, degassing, and eruption style during the explosive–effusive Monte Pilato-Rocche Rosse sequences on Lipari Island.

2. The Monte Pilato-Rocche Rosse sequences

Rhyolite magmas in the Aeolian Islands have been erupting for the last ~55 thousand years (Donato et al., 2006) and over the last ~42 thousand years on Lipari Island. On Lipari, rhyolite eruptive activity is typically cyclic, beginning with an explosive phase and ending with extrusion of obsidian lava flows without a major change in chemical composition (Cortese et al., 1986; Gioncada et al., 2003). The rhyolite explosive and effusive Monte Pilato-Rocche Rosse sequences at the northeastern corner of Lipari Island (Fig. 1) represent the most recent volcanic activity on the island (Cortese et al., 1986; Dellino and La Volpe, 1995) and took place during the sixth century AD (e.g., Dellino and La Volpe, 1995; Lucchi et al., 2010).

The Monte Pilato sequence began with explosive activity forming a large pumice cone (Monte Pilato itself) and the smaller, coeval, parasitic pumice Lami cone on its southern flank (Fig. 1b; Cortese et al., 1986). A small lava body was then erupted in the main crater of Monte Pilato (Tranne et al., 2002). Explosive activity then resumed within the ~1 km wide Monte Pilato crater forming a small tephra cone (Fig. 1b) that corresponds to the Rocche Rosse sequence (Cortese et al., 1986; Dellino and La Volpe, 1995). This later eruptive sequence ended with extrusion of the ~2 km long Rocche Rosse obsidian lava flow that covers the northern slope of the Monte Pilato pumice cone (Cortese et al., 1986) and extends into the sea (Gamberi and Marani, 1997). The small lava flow located below the Rocche Rosse tephra and above the Monte Pilato pumice, and an erosional surface located in the crater walls of the Monte Pilato pumice cone (Fig. 1b) separate the Monte Pilato and Rocche Rosse sequences (Dellino and La Volpe, 1995). Petrographic studies of the explosive and effusive products found that these are nearly aphyric containing only rare microlites of K-feldspar and pyroxene (Gimeno, 2003; Gioncada et al., 2003; Davì et al., 2009; Davì et al., 2010; Clay et al., 2012).

2.1. Eruptive products

Pyroclastic deposits from the Monte Pilato-Rocche Rosse sequences contain alternating layers of phreatomagmatic and purely magmatic

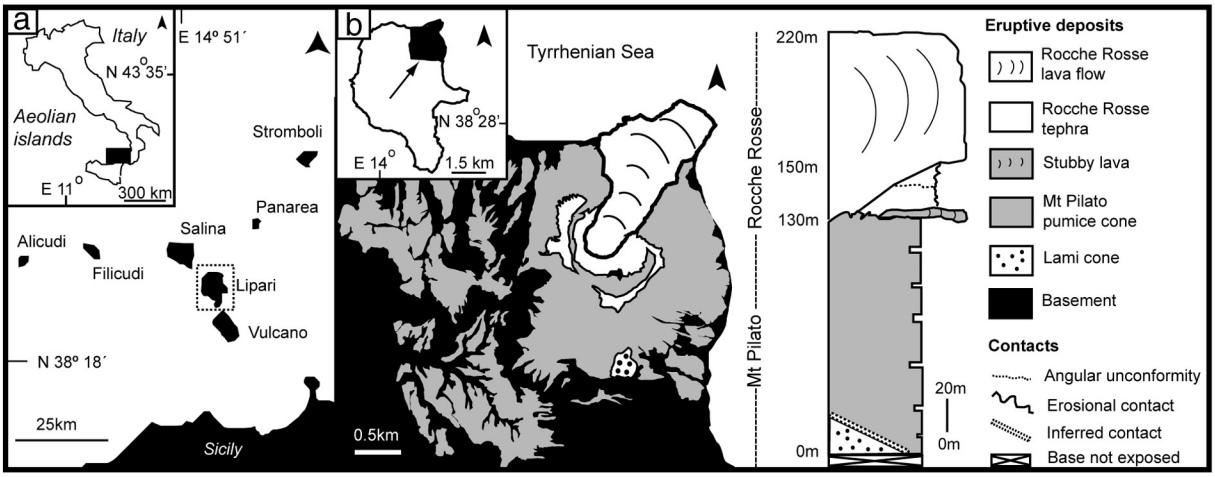

Fig. 1. a) Schematic map of the Aeolian Islands in southern Italy. The box in the left top corner shows the location of the islands, b) Lipari Island in the top left corner and the extension of the Monte Pilato-Rocche Rosse deposits in the centre, modified from Tranne et al. (2002); the box on the right is an idealised lithologic column representing the vertical distribution and contact relationships for the Monte Pilato-Rocche Rosse deposits, modified from Dellino and La Volpe (1995).

tephra (Dellino and La Volpe, 1995, 1996). This study focuses on the magmatic, juvenile products and ignores deposits significantly influenced by external water. The pyroclastic magmatic component is divided into several textural categories: white and grey tube pumice, obsidian clasts including breadcrust bombs, Pele's tears, dense obsidian lapilli and bombs, and tuffisitic obsidian (Fig. 2). Colour differences in tube pumice clasts are attributed to differences in density, where grey tube pumice has a higher density than white (Davì et al., 2011), rather than differences in crystal content or chemistry (Appendix A). The relative proportion of pyroclast types varies with different phases of the eruption. The earlier magmatic deposits related to the Lami cone include white tube pumice pyroclasts, Pele's tear obsidian pyroclasts, and breadcrusted obsidian bombs, with variably fractured and healed glassy rinds (see section 4.2.1 below). The coeval and main explosive Monte Pilato phase includes white tube pumice, scattered dense obsidian, and highly vesicular obsidian pyroclasts. In contrast dense obsidian and tuffisitic obsidian pyroclasts and grey tube pumice were produced by the last explosive phase that formed the Rocche Rosse tephra. Explosive deposits are overlain by the Rocche Rosse lava flow formed by obsidian and variably vesicular and devitrified textural types (e.g., Gimeno, 2003; Clay et al., 2012).

3. Samples and methods

Healed fractures are commonly present in glass forming both explosive and effusive deposits and representative hand samples of a range of textural types were collected. Clasts were cut and polished perpendicular to macroscopic discontinuities and thin sections prepared. Backscattered electron (BSE) images were obtained on a JEOL 840A Scanning Electron Microscope (SEM) at the Monash Centre for Electron Microscopy, Monash University, Melbourne. The SEM was operated at 20 kV accelerating voltage, 15 mm working distance and a probe current of 1×10^{-9} A (see Appendix A for details). Three samples (L01, RRT and Li07-64) were selected for detailed analyses of H_2O content variations in groundmass glass in the vicinity of healed fractures. H_2O contents of pristine glass in 23 samples from explosive and effusive deposits (Table 1) were further analysed using Fourier transform infrared (FTIR) spectroscopy (see below). In order to measure H_2O contents in glass, chips from each sample were prepared into doubly polished wafers with parallel sides ranging in thicknesses from 77 to 1000 μm. The thickness of each wafer was measured with a micrometre with precision of ±5 μm. H_2O contents were measured using benchtop FTIR and synchrotron FTIR (SFTIR) instruments.

Transmission spectra were obtained from obsidian glass in pyroclast interiors, bomb rinds, and from the Rocche Rosse lava flow using a Varian FTS 7000 FTIR Spectrometer at the School of Chemistry, Monash University, and Synchrotron Spectrometer at the Australian Synchrotron. The Monash University bench spectrometer and the Australian Synchrotron FTIR are equipped with an IR microscope and single point and Focal Plane MCT detectors.

In order to determine groundmass glass H_2O concentrations of each sample, H_2O_{mol} and OH^- concentrations were measured using the single point MCT detector interfaced with a KBr beam-splitter. The aperture size was set between 60 and 220 μm. Between 5 and 10 spectra of

Fig. 2. Examples of Monte Pilato pyroclasts: a) white tube pumice, b) foamed obsidian, c) dense obsidian.

Table 1
H_2O content variations in obsidian glass. Lami and Mt Pilato sequences are the oldest, Rocche Rosse the youngest.

Eruptive centre	Facies type	Sample	Detector	Zhang et al. method	σ (±)	3550 peak	σ (±)	Other	n	4520/5230 peak height ratio
Lami	Breadcrust bomb	LO1	Single point	0.68	0.02				12	4
Lami	Breadcrust bomb	LO1	Single point	0.74	0.02				4	3
Lami	Breadcrust bomb	LO1	Array			0.73	0.01		18	
Lami	Breadcrust bomb	LO1[a]	SFTIR	0.76	0.01				10	3.5
Lami	Breadcrust bomb	LO1[a]	SFTIR	0.66	0.00				16	3.5
Lami	Breadcrust bomb	LO2	Single Point	0.89	0.09				3	2.75
Lami	Thin breadcrust bomb	G1	Single point	0.35	0.05	0.4	0.04		7	2
Lami	Pele's tear	Li07-74	Single point	0.27	0.05	0.35	0.03		7	Only 4520
Lami	Pele's tear	LB3	Single point	0.29	0.04	0.31	0.04		7	Only 4520
Lami	Dense	LO3	Single point	0.20	0.002				3	Only 4520
Mt Pilato	Dense	MPO	Array			0.41	0.01		3	
Mt Pilato	Dense	MtPO1	Array			0.20	0.01		5	
RR-tephra	Dense	P50	Array			0.22	0.002		5	
RR-tephra	Vesicular tuffisite	Li07-01	Array			0.33	0.01		5	
RR-tephra	Welded tuffisite	RRT	SFTIR			0.34	0.01		26	
RR lava	Obsidian	Li-08-42	SFTIR			0.13	0.001		80	
RR lava	Obsidian	Li-08-42	Array			0.16	0.02		5	
RR lava	Obsidian	Li-08-42	Single point	0.22	0.001				2	10
RR lava	Obsidian	Li08-06	Array			0.10	0.001		5	
RR lava	Obsidian	Li08-55	Array			0.10	0.001		5	
RR lava	Obsidian	Li08-55	SFTIR			0.12	0.001		6	
RR lava	Macropumiceous	Li07-64	Array			0.23	0.03		9	
RR lava	Dense tube	Li08-12	Array			0.17	0.00		5	
RR lava	Dense tube	Li08-12	SFTIR			0.2	0.01		12	
RR lava	Dense tube	Li07-23	Array			0.06	0.001		5	
RR lava	Dense tube	Li07-23	SFTIR			0.05	0.000		14	
RR lava	Macropumiceous	Li08-17	Array			0.07	0.001		5	
RR lava	Macropumiceous	RRB1	Single point	0.05	0.01				7	Only 4520
RR lava	Micropumiceous	Li08-22	Array			0.06	0.004		5	
RR lava	Micropumiceous	Li08-46B	Single point			0.20	0.02		3	
RR lava	Dyke	Li08-34	Single point			0.09			1	
RR lava	Dyke	Li08-34	Single point			0.21			1	
RR lava	Obsidian	P3RR-33[b]						0.21		
RR lava	Obsidian	P3RR-120[b]						0.15		
RR lava	Obsidian	OISd[c]						0.26	3	
RR lava	Obsidian	30A[c]						0.1	3	
RR lava	Pumiceous	1C[c]						0.13	3	
RR lava	Pumiceous	30C[c]						0.06	3	

[a] Cabrera et al., 2011.
[b] Gottsmann and Dingwell, 2001.
[c] Davi et al., 2010.

128 scans each were acquired, on different spots on each wafer using a white light source. Straightline baselines were used to calculate peak heights. Glass density was taken to be 2370 kg/m^3. H_2O concentrations were determined in two different ways: (1) from the intensity of the broad 3570 cm^{-1} absorption band using the Beer–Lambert law as in Newman et al. (1986) and using an absorption coefficient of 80 L/mol cm^{-1} (Ihinger et al., 1994), and (2) from the intensities of the 4500 cm^{-1} and 5200 cm^{-1} absorption bands for those samples with saturated or oddly shaped peaks at 3570 cm^{-1}. Where both the peak at 3570 cm^{-1} and the pair of peaks at 4500 and 5200 cm^{-1} were used, calculated H_2O concentrations are consistently higher using the 3570 cm^{-1} peak than using the 4500 and 5200 cm^{-1} peaks, but are within uncertainty limits of each other (Table 1). Total H_2O concentration (H_2O_{total}) was calculated using these near-IR absorption peaks according to the calibration technique of Zhang et al. (1997). Peak heights were commonly ~3 times greater for the OH^- peak (4500 cm^{-1}) than the H_2O peak (5200 cm^{-1}; Table 1). Further, for those samples with heterogeneous textures (e.g., healed fractures and truncation planes), the 64 × 64 pixel focal plane array detector at the School of Chemistry, Monash University was used, with pixel size of 5.5 μm, and resulting in a single tile, 352 × 352 μm raw array H_2O map image. For each tile we acquired 128 scans. H_2O_{total} concentrations were determined from the intensity of the broad 3570 cm^{-1} absorption band as above. Errors associated with thickness measurements or microlite influences are smaller than variation for repeated measurements through different techniques. Average and standard variations of measurements for each analysed area of samples are noted in Table 1. Although measured H_2O concentrations have standard deviations of up to ±0.09 wt.% H_2O, measurements were not repeated in the exact same spot and do not calculate errors related to absorption coefficient and baseline fit; a conservative relative uncertainty value of ±10% (Castro et al., 2008; Tuffen et al., 2010) is herein adopted.

In order to display H_2O concentration variations in glass, 2D raw data array H_2O maps were converted into 2D or 3D images using Bruker Optus version 6.5 and Varian Resolution Pro 4.0 softwares. Each array map varies between one single tile (352 × 352 μm) and up to 5 horizontally or vertically aligned tiles (352 × ~1056 μm, sample Li07-64). Furthermore, SFTIR H_2O transects were assembled into rectangular point H_2O maps using multiple single point measurements, within areas up to 80 μm wide and 1840 μm long. For methodology see Cabrera et al. (2011). Transects and measurements are spaced every 10 μm (sample RRT), or 40 and 60 μm (sample LO1). 128 scans for each spectrum were used and the background measured every 5 measurements. Blue and green colours represent areas where IR absorption peak heights for H_2O bands were minimum and yellow to red colours correspond to areas where maximum values were obtained.

4. Results

Here we summarize whole-rock chemistry and H_2O concentrations of different types of eruptive rocks and then describe typical microstructures of these rocks that suggest multiple ways and times during the eruption in which melt underwent fracturing and healing. The final subsection describes H_2O concentrations around healed fractures.

4.1. Whole-rock chemistry and H_2O concentration

Whole rock compositions of juvenile material from explosive and effusive phases are within error of each other (Appendix A and Gottsmann and Dingwell, 2001; Gioncada et al., 2003; Davì et al., 2010; Cabrera et al., 2011; Davì et al., 2011; Clay et al., 2012). Samples are all rhyolitic in composition, and the glass contains an average of 74.4 ± 0.3 wt.% SiO_2. Furthermore, both explosive and effusive juvenile clasts (excluding devitrified areas of the lava flow) are crystal-free with less than ~1 vol.% microlite needles of pyroxene and feldspar. Significant differences were found for the dissolved H_2O concentration in glasses. Maximum H_2O concentration is greater in samples from explosive phases (0.9 wt.%) than from effusive phases (0.26 wt.%; Table 1 and Fig. 3). Carbon dioxide concentrations, in all cases, were below detection.

The explosive Lami cone, the earliest in the sequence of events, contains samples with wide variations in H_2O concentration depending on clast type (Figs. 3 and 4). Glasses from pyroclasts that dominate the cone-building phase of the eruption are relatively H_2O-rich. These pyroclasts remained ductile after their fragmentation and deposition. The glassy rind of breadcrusted obsidian pyroclasts with highly-vesiculated interiors has H_2O concentration varying between ~0.6 and 0.9 wt.%, whereas glass from Pele's tear pyroclasts varies between 0.27 and 0.35 wt.%. These values contrast with those measured in a dense obsidian pyroclast from the same eruption with only 0.20 wt.% (sample L03 in Fig. 3 and Table 1).

Glass from dense obsidian pyroclasts of the simultaneously active Monte Pilato vent has a similarly low H_2O concentration, between 0.20 and 0.41 wt.%. The last explosive eruption that formed the Rocche Rosse tephra deposits is characterized by dense obsidian and tuffisitic obsidian glasses (samples Li07-1 and RRT in Fig. 3 and Table 1), which have H_2O concentrations between 0.22 and 0.34 wt.%.

Glass samples from the Rocche Rosse lava flow, the latest in the sequence of events, have the lowest measured H_2O concentrations of 0.10 to 0.26 wt.% (Fig. 3). Similarly, glass from highly vesicular material in the carapace of the lava flow and hinge zones of large flow folds vary from 0.23 to 0.05 wt.% H_2O. These results reproduce the same range of values obtained by FTIR (Gottsmann and Dingwell, 2001; Davì et al., 2010) and secondary ionization mass spectrometry (Clay et al., 2012) recorded for glass on the Rocche Rosse lava flow.

4.2. Microstructures in fractured and healed obsidian

Fracturing of obsidian is documented in the different types of pyroclasts and lava flow. Healing tends to erase evidence for fracturing, but displacement of pre-existing features across the fracture plane, together with dusty particles on the plane, makes fractures obvious.

4.2.1. Breadcrusted and tuffisitic obsidian pyroclasts

A breadcrusted obsidian bomb from the Lami cone shows a single planar micro-fault in its rind. The fault truncates folded micro-vesicle and microlite-rich bands (~1% needles of very thin and <100 μm long pyroxene) and pristine glassy bands (Fig. 4a, b; Cabrera et al., 2011).

Single planar faults are also present in dense tuffisite (clastic material) glass from pyroclasts in the Rocche Rosse tephra. For example, sample RRT contains a healed fault that offsets tuffisite bands (Fig. 4c–e). The fault trace is highlighted by a dusty brown colour due to a concentration of small <10 μm opaque microlites (Fig. 4e). The fault trace is crenulated and crenulations are asymmetric, which combined with drag folding of banding on the glass on either side of the fault, indicates sense of movement and that the glass resumed its viscous behaviour after faulting (Fig. 4e).

Two types of tuffisite are present within obsidian pyroclastic samples from the Rocche Rosse tephra deposits: *vesicular tuffisite* and *banded tuffisite*. Vesicular tuffisite contains narrow tuffisite bands in pyroclasts with both dense obsidian and pumiceous domains. In the sample in Fig. 5, vesicular tuffisite bands cut across a block-sized pyroclast. The bands are up to 1 cm wide and filled with grey, clastic glassy matrix <1 mm in particle size surrounding elongated black obsidian clasts that vary in length from millimetres to 1 cm. In some cases, obsidian clasts are broken up into fragments with a jig-saw fit pattern (Fig. 5c). These dense clasts are oriented parallel to tuffisite band margins and have asymmetric shapes indicative of shearing, marked by curved foliation in the fine matrix wrapping around the clasts (Fig. 5a). Both dense and pumiceous textural domains surround the tuffisite bands. However, dense veneers around pumiceous domains and separating pumice from tuffisite suggest that vesiculation in pumiceous domains occurred after tuffisite formation (Fig. 5a,b).

In contrast, banded tuffisite (Fig. 6) forms disconnected lenses or irregular and connected grey bands in hand-specimen (Figs. 4c and 6a) separated by lenses or bands of clean, microlite-free obsidian (black in hand specimen) or jig-saw fit angular clasts (Fig. 6c). Banded tuffisite lacks vesicular domains. Tuffisite in these clasts is comprised of brown glass, rich in opaque microlites and small clasts of transparent glass

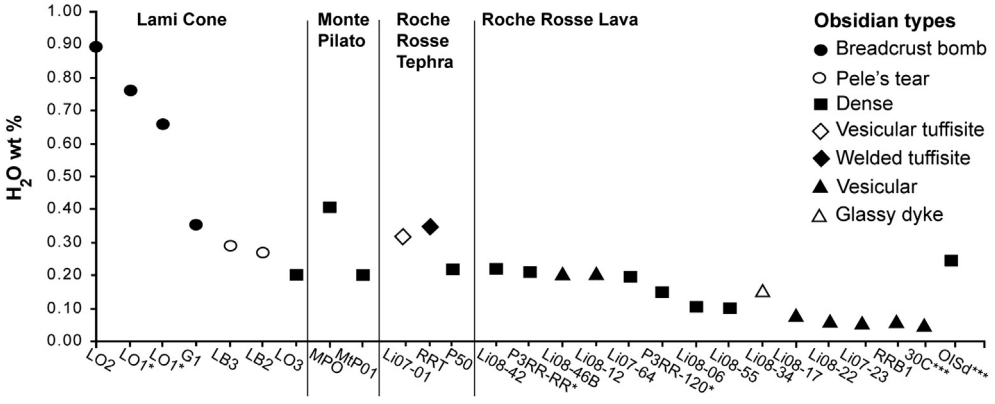

Fig. 3. H_2O content of samples from the different eruptive centres corresponding to the Monte Pilato-Rocche Rosse sequences and related textural product types. Letters and numbers on horizontal axis are sample labels, vertical lines separate eruptive centres and tephra vs. lava from the same eruption. * = FTIR H_2O values from Cabrera et al. (2011); ** = FTIR H_2O values from Gottsmann and Dingwell (2001); and *** = FTIR H_2O data from Davi et al. (2010).

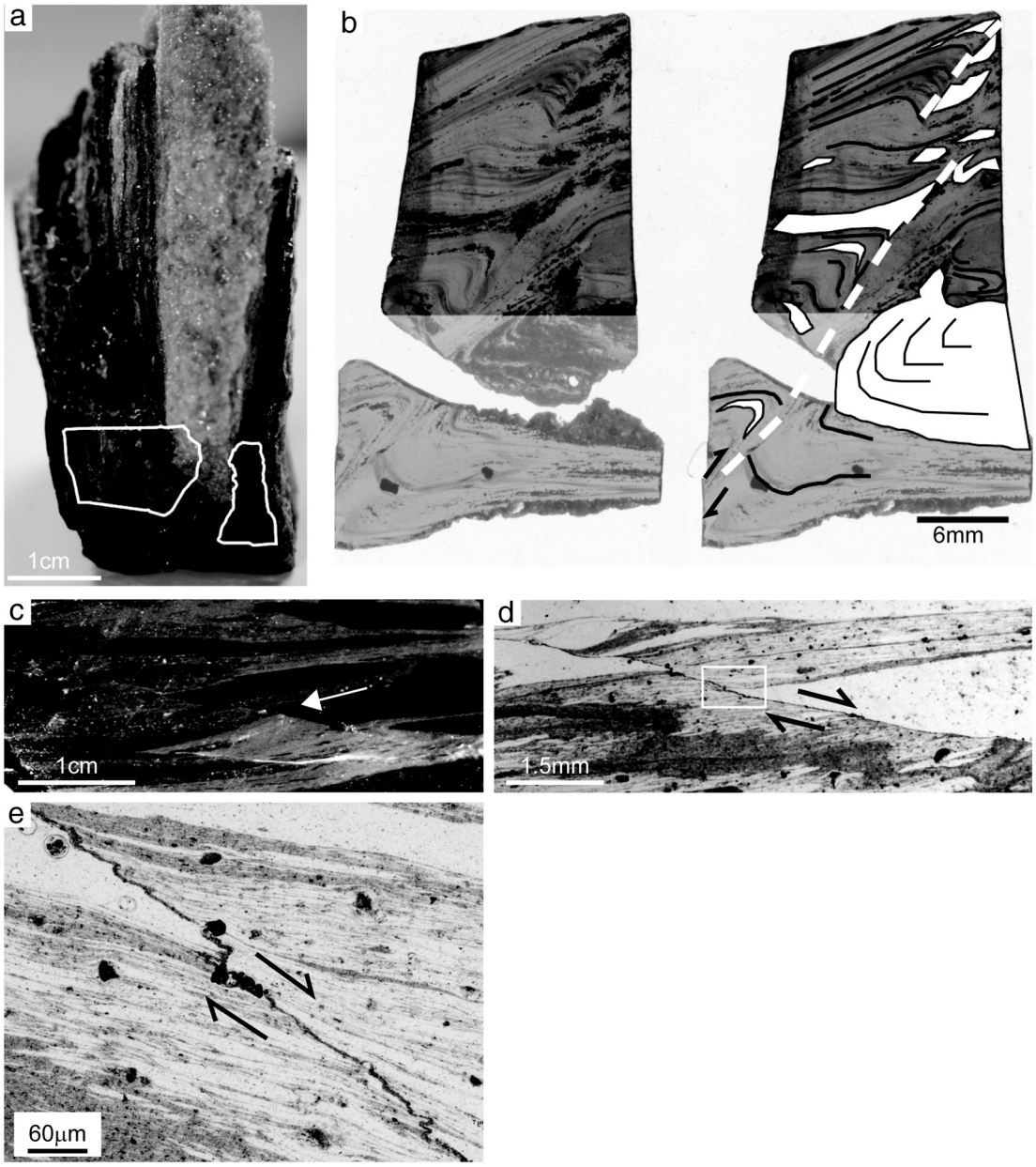

Fig. 4. Healed faults in obsidian glass. a) Edge of a breadcrusted obsidian pyroclastic bomb from Lami cone (sample RRT). Black is obsidian glass and white is vesiculated glass. White lines depict the shape and position of the two wafers in (b). b) 900 and 1000 μm thick wafers from pyroclast in (a) covering parts of a 3 cm-long fault. Light grey is clean glass, dusty bands are microlite-rich glass, and black irregular patches are vesicles and voids. On the right-hand-side, interpretative black lines represent microlite-rich bands, and white polygons indicate vesicle-rich domains. Note vesicles concentrated at the hinge of drag folds. White dashed line marks position of fault and black half-arrows indicate movement sense. c) Fault (white arrow) in obsidian pyroclast from Rocche Rosse tephra. Black bands are obsidian and grey bands are tuffisite. d) Scanned thin section of (c), white is obsidian, and grey is tuffisite. Note truncation, dragging and displacement of bands by fault. White square marks the area shown in (e). e) Detail of (d) showing truncation and displacement of tuffisite and obsidian bands across a crenulated fault plane. Crenulation of fault plane indicates resumption of viscous behaviour after faulting. Half arrows in (d) and (e) indicate movement sense on fault interpreted from asymmetric crenulation and dragging of banding.

(Fig. 6b–e). The edges of each transparent glass lens are well-defined by concentrations of opaques, whereas interiors are clean. Both glass types form lenses with their longest axes varying in length from ~50 μm to ~3 mm. The distribution of lenses in Fig. 6 is complex in detail. In some areas, lenses of brown dusty glass are surrounded by transparent glass (Fig. 6b). In other areas, the opposite is true (Fig. 6c). In Fig. 6d, angular transparent, clasts are hosted by brown glass matrix, which in turn forms a separate clast within transparent obsidian. Commonly, the two types of glass are found as long, thin bands that show complex folding structures (Fig. 6e). As exemplified by the sample in Fig. 6, the definition of matrix and clast in banded tuffisite depends on scale. The two glass types are mingled at various scales, fractured, folded, and stretched into long lenses (see Section 5).

4.2.2. Obsidian lava flows

Obsidian from the Rocche Rosse lava flow commonly exhibits multiple micro-fault sets showing both planar and crenulated faults (Fig. 7). The northwestern edge of the Rocche Rosse lava flow front is also cut by *subplanar breccia zones* (Fig. 8). Road cut exposures demonstrate that the breccia bands persist for at least ~20 m into the lava body and maintain a consistent ~N350/30E orientation. Breccia bands are ~1 m wide and continuous for up to 6 m (Fig. 8a) near the flow margin.

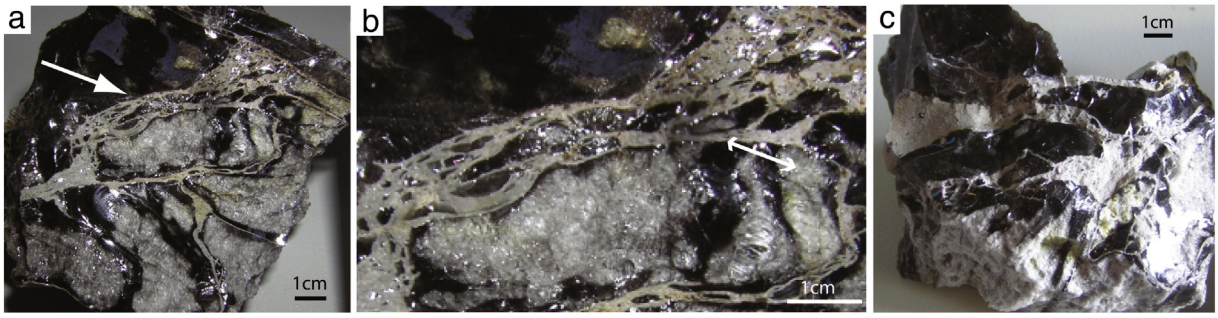

Fig. 5. *Vesicular tuffisite* obsidian pyroclast from Rocche Rosse sequence: a) fragment of a large (~1 m) obsidian pyroclast containing light grey tuffisite bands that include elongate and asymmetric obsidian clasts. Morphology of these clasts indicates shearing wrapped by foliation in fine matrix (sample Li07-01). b) Enlargement of (a). Vesicles in pumiceous domains are elongated parallel to the double-pointed arrow on the right-hand-side of image. We interpret these features to indicate stretching of low pressure, vesiculated bands. c) In some cases, obsidian clasts in tuffisite preserve jig-saw fit textures.

Towards the interior of the lava, bands narrow, varying from ~3 cm to ~40 cm wide, and are continuous for up to 2 m. The bands consist of angular to elongated and welded clasts in a finer clastic glassy matrix bordered by localised bands of dark blue to brown banded obsidian concentrated near the breccia zone walls. Breccia contents are similar in composition and texture to tuffisite in pyroclasts, although clasts reach larger sizes in breccia bands than in tuffisite. Clasts within breccia bands are generally oriented parallel to fracture walls and vary in size from lapilli to block-size (Fig. 8b). Clasts are variably vesicular and variably devitrified. Abrasion of breccia margins during fracturing of the lava is evidenced by preservation of different stages of break-up of wall clasts (Fig. 8b). Doubly polished wafers of the obsidian matrix reveal high aspect ratio vesicles (>100 μm long and <10 μm across, Fig. 8c) defining foliations that are truncated by sharp fault surfaces (Fig. 8d) and flow folds (Fig. 8e).

4.3. Microstructures in fractured and healed pumice

Pumice pyroclasts show distinct domains characterized by vesicles of different orientation or aspect ratio in 2D sections (Fig. 9). Boundaries between these domains may be more or less sharp (compare differences in Fig. 9). Fig. 9c shows three bands of strongly elongated vesicles forming tube pumice (top, middle and bottom) interlayered with two bands of moderately to weakly elongated vesicles with stair-stepping foliation, containing kernels where vesicles are roughly circular. Banded microstructures are interpreted to represent zones of high strain interlayered with zones of low strain. The asymmetry of the foliation in Fig. 9c indicates shear in a top-to-the-left direction.

4.4. H_2O distribution around fractures

SFTIR and FTIR 3D maps of H_2O concentrations across healed fractures in pyroclastic and effusive obsidian define V-shaped troughs of low H_2O content coincident with fracture planes (Fig. 10). In pyroclastic obsidian sample LO1-Lami, H_2O varies from 0.66 and 0.73 wt.% on either side of the fault trace, to a low of 0.61 wt.% at its trace (Fig. 10a and b). Single point FTIR H_2O content measurements on either side of healed fractures in different areas of the same sample show a broadly similar pattern. Similarly, the trace of healed faults in the glass from the late Rocche Rosse lava flow sample Li07-64 in Fig. 7 defines H_2O content troughs (Fig. 10c–f). Interestingly, H_2O profiles in the vicinity of the two faults are similar and decrease to a low of 0.12 wt.% in the fault plane (Fig. 10d–e).

Fig. 11 shows a SFTIR H_2O transect that crosses both the brown, dusty tuffisite and the clean, microlite-free obsidian bands in a banded tuffisite. As is common, the brown glass hosts smaller and elongated clasts of transparent obsidian (Fig. 6). H_2O content decreases gradually from 0.34 and 0.29 wt.% in the transparent and clast-free obsidian lenses, to 0.26 wt.% at the centre of the clast-rich brown obsidian breccia.

5. Discussion

The Monte Pilato-Rocche Rosse sequence evolved from explosive to effusive eruptions and the products of eruption include obsidian with variable dissolved H_2O contents reaching very low values, and include healed fractures at many scales (e.g., Tuffen and Dingwell, 2005). In this section, we discuss evidence for fracture and healing processes and degassing during fracturing. Our results support models suggesting that fracturing of magmas in conduits can explain both the formation of volatile-poor, vesicle-free obsidian (Yoshimura and Nakamura, 2010; Cabrera et al., 2011) and the decrease in explosivity during a typical eruptive cycle (e.g., Gonnermann and Manga, 2005).

5.1. General features of obsidian in the Monte Pilato-Rocche Rosse sequences

5.1.1. Repeated fracturing and healing

Like high-silica rhyolite glasses erupted elsewhere, obsidian from the Monte Pilato-Rocche Rosse explosive eruptions is richer in H_2O than the effusive counterpart (Fig. 3). Given similar whole-rock major element compositions of explosive and effusive products (Appendix A), it is most likely that magmatic volatile content controlled the change in eruption style (e.g., Newman et al., 1988; Villemant and Boudon, 1998). Microstructural features documented above indicate that melts forming the eruptive Monte Pilato-Rocche Rosse products underwent multiple brittle–ductile transitions during emplacement and that degassing due to fracturing may have played an important role in the decreasing explosivity of the eruptive sequence.

Evidence for multiple brittle–ductile transitions in a single sample is demonstrated by healed and crenulated fault planes in pyroclasts (e.g., Fig. 4). This indicates that the melt resumed viscous flow after faulting, leading to crenulation (Fig. 4e). Repeated crossing of the glass transition in this manner implies a strain-rate dependent rheological transition (as opposed to strictly temperature-dependent transition). We infer that strain rate variations thereby led to in-conduit brecciation, as recorded by vesicular and banded tuffisites (Figs. 5 and 6). Vesicular tuffisite (Fig. 5) marks brecciation and local vesiculation interrupted by ejection. Banded tuffisite (Fig. 6) records multiple brecciation events followed by resumption of viscous flow, giving rise to a "stretched and folded" and rather cryptic breccia in the conduit. Similarity to microstructures from other rhyolite deposits suggests that multiple events of silicic magma fracturing and healing might be a general process (Rust and Cashman, 2007) and that these could result in typical flow banding characteristic of obsidian (Tuffen et al., 2003; Tuffen and Dingwell, 2005) as supported by models (Gonnermann and Manga, 2005).

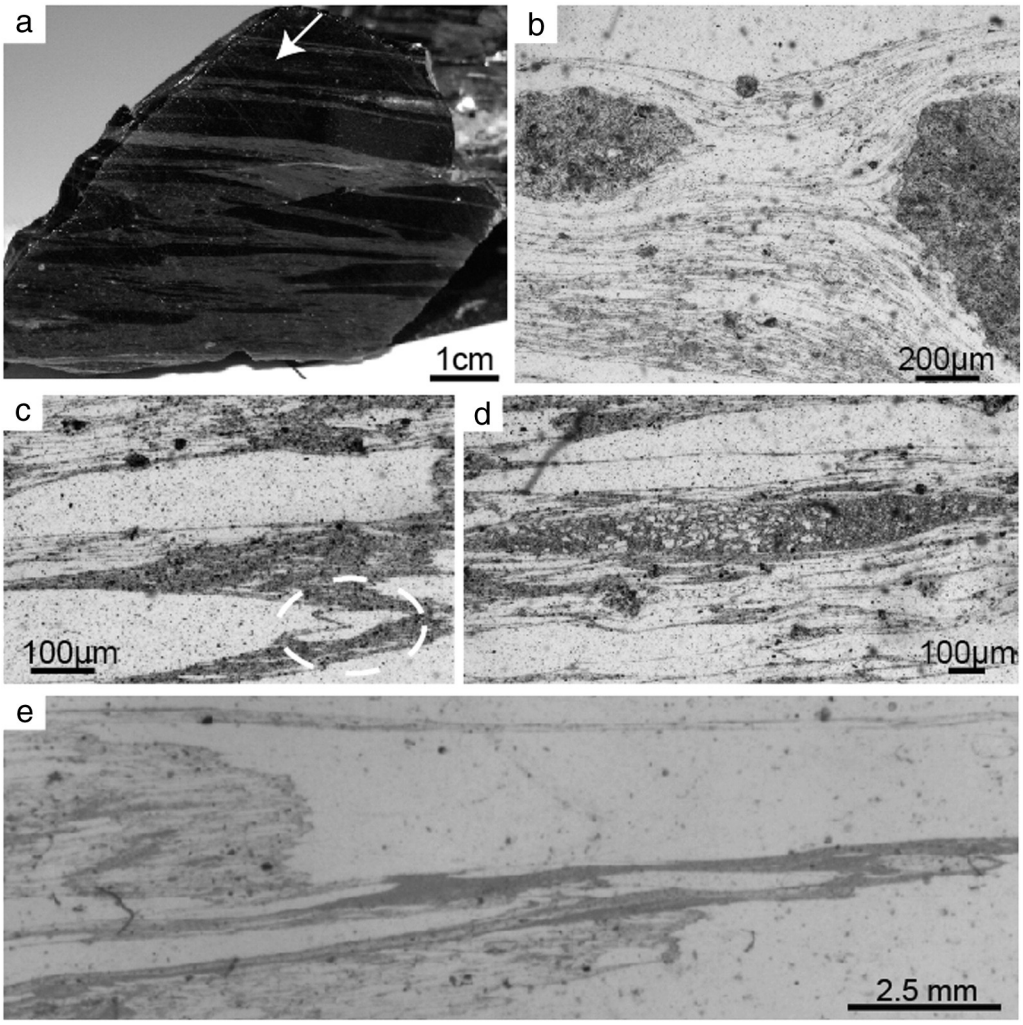

Fig. 6. *Banded tuffisite* obsidian pyroclasts, Rocche Rosse sequence: a) hand specimen of obsidian pyroclast, sample RRT, with black obsidian bands and grey clastic bands (tuffisite). (b) to (f) are photomicrographs from sample in (a). b) Brown dusty clasts rich in oxide microlites surrounded by light grey, clean regions of oxide-free glass. Fine bands define flow into a pressure shadow around the dusty clasts. c) Brown dusty matrix with large and small clean white clasts. Dashed circle depicts jig-saw fit in situ fragmentation. d) Elongated large white and brown dusty clasts/domains. Brown clasts host smaller white fragments. e) Complex folding and stretching of both white and dusty clasts. Combined, microstructures suggest that the two types of melt (dusty brown and clear obsidian) were multiply brecciated, where the strained aspect of clasts, particularly in (e), suggest post-brecciation flow.

Brecciation is not restricted to non-vesicular regions of melt; vesicular material (foams) also experienced multiple fracture events. Pumice pyroclasts have line-sharp planes that separate distinct microstructural domains, where domains vary in vesicle elongation direction and aspect ratio (tube pumice in Fig. 9a–b and d) or in degree of strain

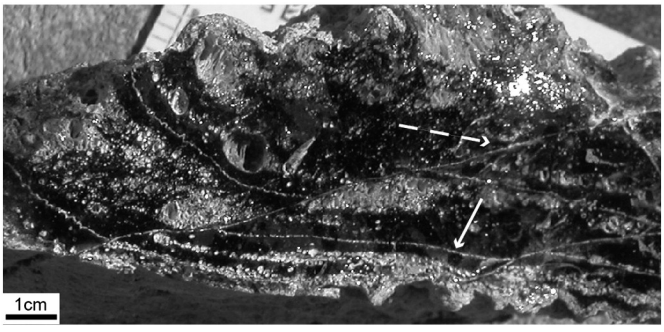

Fig. 7. Faults in sample of dense obsidian Li07-64 from Rocche Rosse lava flow. Black is obsidian, vesicle-rich bands are white and thin, crenulated white lines are different fault sets. White sub-horizontal crenulated lines are early faults (continuous arrow) that together with vesicle-rich bands are displaced by two later faults from upper right to lower left (dashed arrow).

(banded pumice with asymmetric vesicles, Fig. 9c; Wright and Weinberg, 2009). These microstructures could have formed in two ways: a) fragmentation of foam into individual clasts and subsequent healing in the conduit (Fig. 9a–b and d) (Tuffen et al., 2003; Tuffen and Dingwell, 2005), or b) strain localization into narrow shear zones where stresses exceed the yield strength for foams (Fig. 9c; yield behaviour is characteristic of foams, e.g., Weaire, 2008). These microstructures in tube pumice pyroclasts on Lipari (see also Wright and Weinberg, 2009) are comparable to those in pumice clasts from the Cordón Caulle, Chile 2011–2012 eruptions (Schipper et al., 2013), Vesuvius 79 A.D. (Shea et al., 2012), and to those experimentally reproduced from sheared silicic foams (Okumura et al., 2010). Brecciation and healing or strain localization in silicic foams with yield strength may therefore be general features of eruptive activity (Okumura et al., 2010; Castro et al., 2012b; Shea et al., 2012; Schipper et al., 2013). In-conduit brecciation of pumice may represent events where the fragmentation threshold of the vesicular magma was exceeded locally but not globally, and thereby was insufficient to produce an explosive eruption (cf. Spieler et al., 2004).

Evidence for fracturing and healing is also present in the Rocche Rosse lava flow. Here too, obsidian from the lava flow records early crenulated and healed micro-fractures displaced by sets of later faults (Fig. 7) indicating a crossing of the glass transition at least twice. At

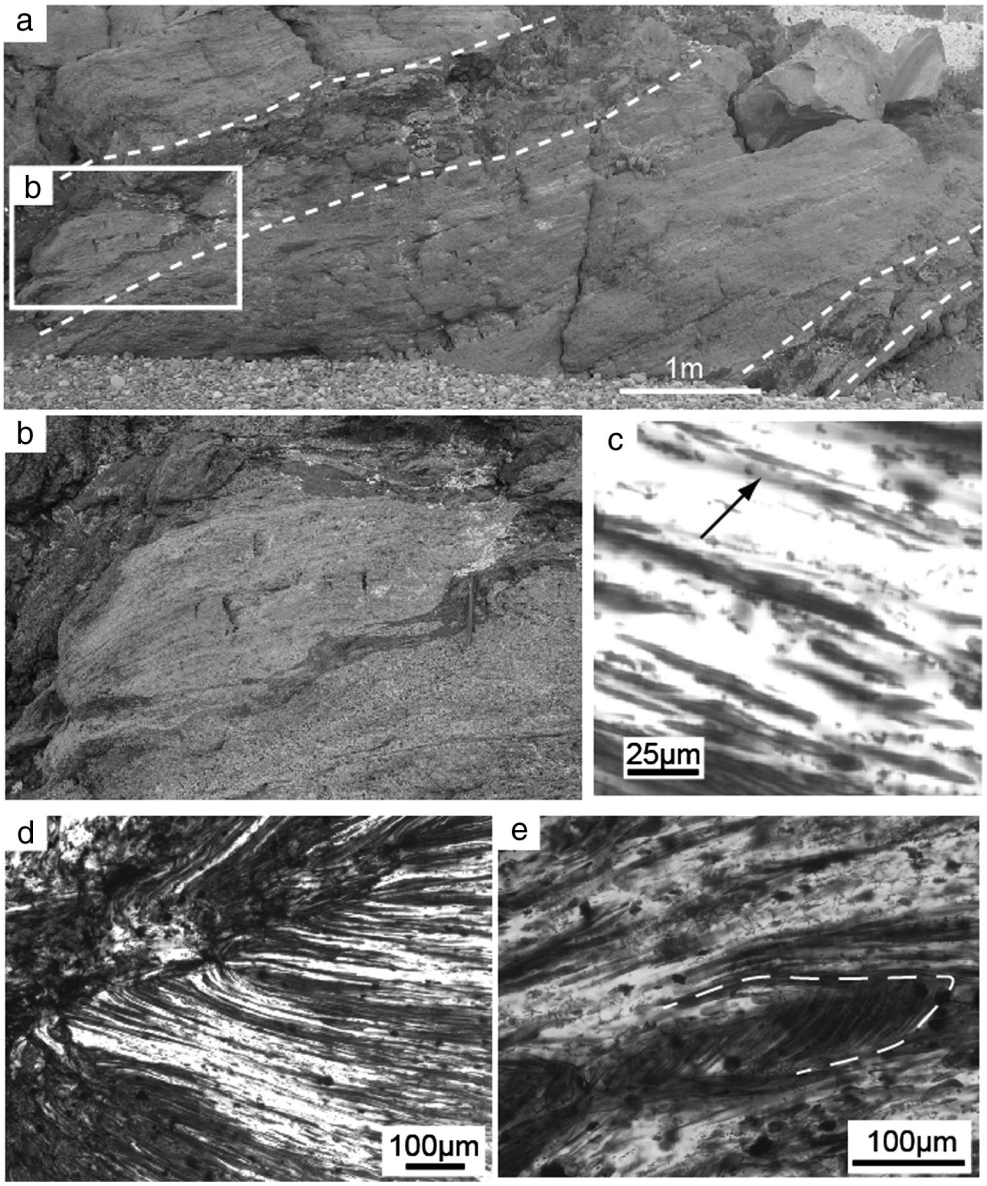

Fig. 8. a) Subplanar breccia zones marked by dashed lines in the flow front of the Rocche Rosse lava flow (2 km away from vent, in the vicinity of Aquacalda). Breccias are composed of welded clastic material derived from abrasion of the walls. Clasts are elongate and irregular in shape. Rectangle indicates location of (b). b) Large (~1.5 m long) devitrified obsidian clast at the wall of the breccia zone broken in situ into smaller clasts. c–e) Photomicrographs (plane polarized light) of obsidian matrix. White (transparent) is glass, black is oxides. Arrow in (c) points to an elongated vesicle (in 2D). Small dark ellipses are high aspect ratio micro-vesicles and thin brown lines are concentrations of elongate micro-vesicles in 2D. Note truncation planes in (d) and tight folds in (e) indicated by white dashed line.

the macro-scale, parts of the lava fractured into metre-long clasts that were included in the flowing magma within breccia planes (Fig. 8b). The obsidian matrix in these subplanar breccia zones has microstructures suggestive of rapid emplacement, such as the strongly elongated vesicles (Fig. 8c), folding of obsidian bands (Fig. 8e), as well as fracturing and healing (Fig. 8d).

5.1.2. H_2O loss associated to melt fracturing

In the previous section, we discussed microstructural evidence for multiple fracturing and healing events during conduit flow and extrusion, and of both highly vesicular (Figs. 5 and 9) and dense (Figs. 4 and 6) magma. Melt fracturing is a general feature. In this section we discuss evidence that fracturing is accompanied by degassing.

The link between faulting of glass in the conduit and H_2O loss has been documented here and in other studies (Cabrera et al., 2011; Castro et al., 2012b; Shea et al., 2012; Watkins et al., 2012). Profiles presented here show H_2O loss of up to 0.14 wt.% towards single fractures in pyroclasts and lava samples (Fig. 10) as well as tuffisite bands in the stretched breccias formed in the conduit (Fig. 11). H_2O troughs across healed faults indicate that H_2O escaped while fractures were still open and hot (Fig. 10a–b). The drop in water content indicates that fracturing gave rise to low pressure or local increase in temperature, possibly due to friction, causing H_2O diffusion from the glass into the fracture (Cabrera et al., 2011). Pressure or temperature inside the fracture cannot be gauged accurately from the H_2O content curve, because P–T could fluctuate over time scales too short to allow H_2O content equilibration, and because H_2O content changes during fracturing will be at least partly homogenized by post-healing H_2O diffusion (Yoshimura and Nakamura, 2010; Cabrera et al., 2011). Fractures remain open for an undetermined time, which depends upon relative pressure within the fracture, translation and rotation of fragments, and timescale to heal juxtaposed surfaces, which is itself dependent upon temperature and roughness of the fracture surface (Yoshimura and Nakamura, 2010). However long the fractures remained open, the

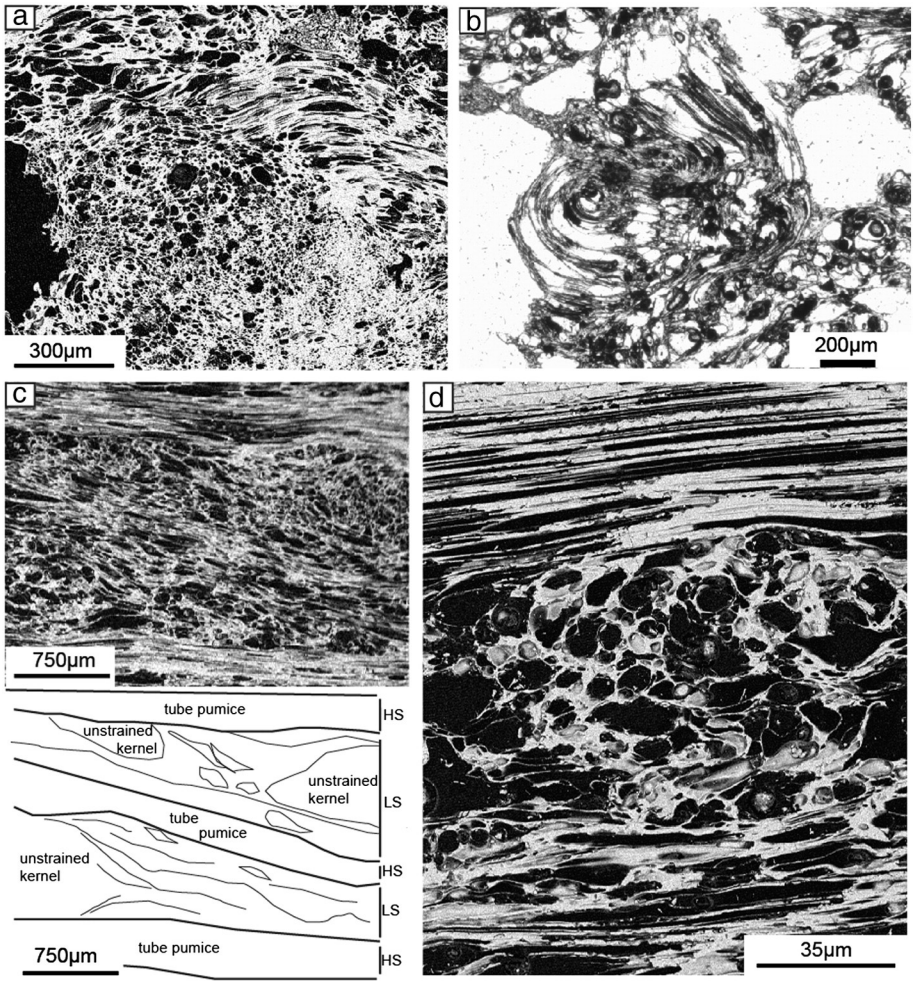

Fig. 9. Sharp discontinuities between microstructural domains in pumice pyroclasts in 2D. a) Backscattered electron (BSE) image of a pyroclast from Rocche Rosse sequence: an irregular band of sheared vesicles in the top third of photomicrograph showing asymmetry indicative of top-to-the-right movement, sharply separated from a region below of roughly circular vesicles. b) Photomicrograph (plane polarized light) of a pyroclast sample from Lami cone: stretched and folded vesicles define a spiral surrounded by zones of roughly circular vesicles. (c) BSE image of Monte Pilato tube pumice pyroclasts: three bands of strongly stretched vesicles (high strain zones, HS) forming tube pumice (top, middle and bottom) interlayered with two bands of moderately to weakly stretched vesicles with stair-stepping foliation (low strain zones, LS) indicative of shearing with top-to-the-left movement sense. Note three kernels in these two bands where vesicles are rounded. Line drawing shows interpretation of image, including asymmetric vesicles. d) BSE image of same sample as (c) showing a sharp boundary above and below a central kernel with circular vesicles. Sharp changes in vesicle aspect ratio between domains suggest regions with different strain histories interpreted to represent re-healed pumice clasts.

presence of crenulated healed faults (Figs. 4e and 7) suggests that the glass was sufficiently hot to flow after fracturing.

Decrease in H_2O content of glass across banded tuffisite from the Rocche Rosse tephra (Fig. 11) is continuous from the centre of a nonvesicular obsidian domain to the most intensely brecciated clastic band (from left to right in Fig. 11). We suggest that this H_2O profile is the result of H_2O loss during syn-eruptive brecciation in the conduit, with maximum loss where fracturing was most intense, as marked by fine clastic material (see also Rust and Cashman, 2007; Stasiuk et al., 1996; Tuffen et al., 2010). The H_2O profile has been smoothed after healing by diffusion while the material was still hot (cf. Castro et al., 2005; Yoshimura and Nakamura, 2008 and 2010). Castro et al.

Fig. 10. Healed fractures in pyroclastic obsidian from Lami and Rocche Rosse lava flow and associated H_2O content variations. a) Thick wafer from sample L01-Lami (shown in Fig. 4; see also Fig. 5b and Cabrera et al., 2011). Dashed line marks a fault that truncates banding. Black circles and values mark three selected synchrotron FTIR measurements of H_2O content with a minimum at the fault (0.61 wt.%). Black arrows indicate movement sense on fault; white arrow highlights a devitrified healed glassy clast. b) Raw SFTIR molecular H_2O distribution from the 5200 cm^{-1} absorption band corresponding to two transects plotted side-by-side as a single band (Cabrera et al., 2011) across fault in (a). Black dots mark position of the three values in (a). c) Rocche Rosse lava flow: wafer 120 μm thick, from sample in Fig. 7, marking position of FTIR transects across two faults (black lines). Medium grey is obsidian and light grey are open vesicles. Black marks oxides. White rectangle shows the position of the 64 × 64 pixel focal plan array H_2O maps with a pixel size of 5.5 μm shown in (e) and (f). d) 3D representation of H_2O concentration distribution. H_2O content variations define two troughs spatially coincident with the trace of the two faults shown in (c) area 1 covered by the two black lines. Area is a mosaiced tile 700 × 352 μm obtained by the 64 × 64 MCT Focal Plane Array detector. Colours represent different H_2O contents according to IR absorption peak heights for the 3570 cm^{-1} absorption band. Blue and green colours represent minimum values and yellow to red colours represent maximum values. Narrow positive red peaks correspond to Fe-Ti oxides in glass. (e) Plan view image of the raw data of H_2O content variation. The two numbered points indicate absolute values of H_2O content. Red box is a zoom into the healed fault trace shown in (f). f) Photomicrograph of the area highlighted by white rectangle in (c). Grey is obsidian, black is devitrified products, and random black points are oxides. Fracture plane is discontinuous and marked by concentration of black oxides. For interpretation of the references to colour in this figure legend, the reader is referred to the web version of this article.

(2012b) found that glass of vesicular tuffisite pyroclasts from Chaiten also has maximum H_2O loss linked to fractured areas (e.g., Fig. 3b in Castro et al., 2012b). Similar to our results, Rust and Cashman (2007) found H_2O variations of up to 0.25 wt.% amongst healed clasts in welded breccia from pyroclastic deposits at Newberry Volcano. They interpreted that shearing and flowing of rising magma could have brought together clasts from different areas of the conduit.

5.2. Melt fracturing, degassing and decreasing explosivity of rhyolite eruptions

Degassing through fractures inhibits explosive fragmentation by inhibiting the formation and growth of bubbles (Yoshimura and Nakamura, 2010), increasing the pressure difference necessary for explosive fragmentation (Spieler et al., 2004). The textural, structural and

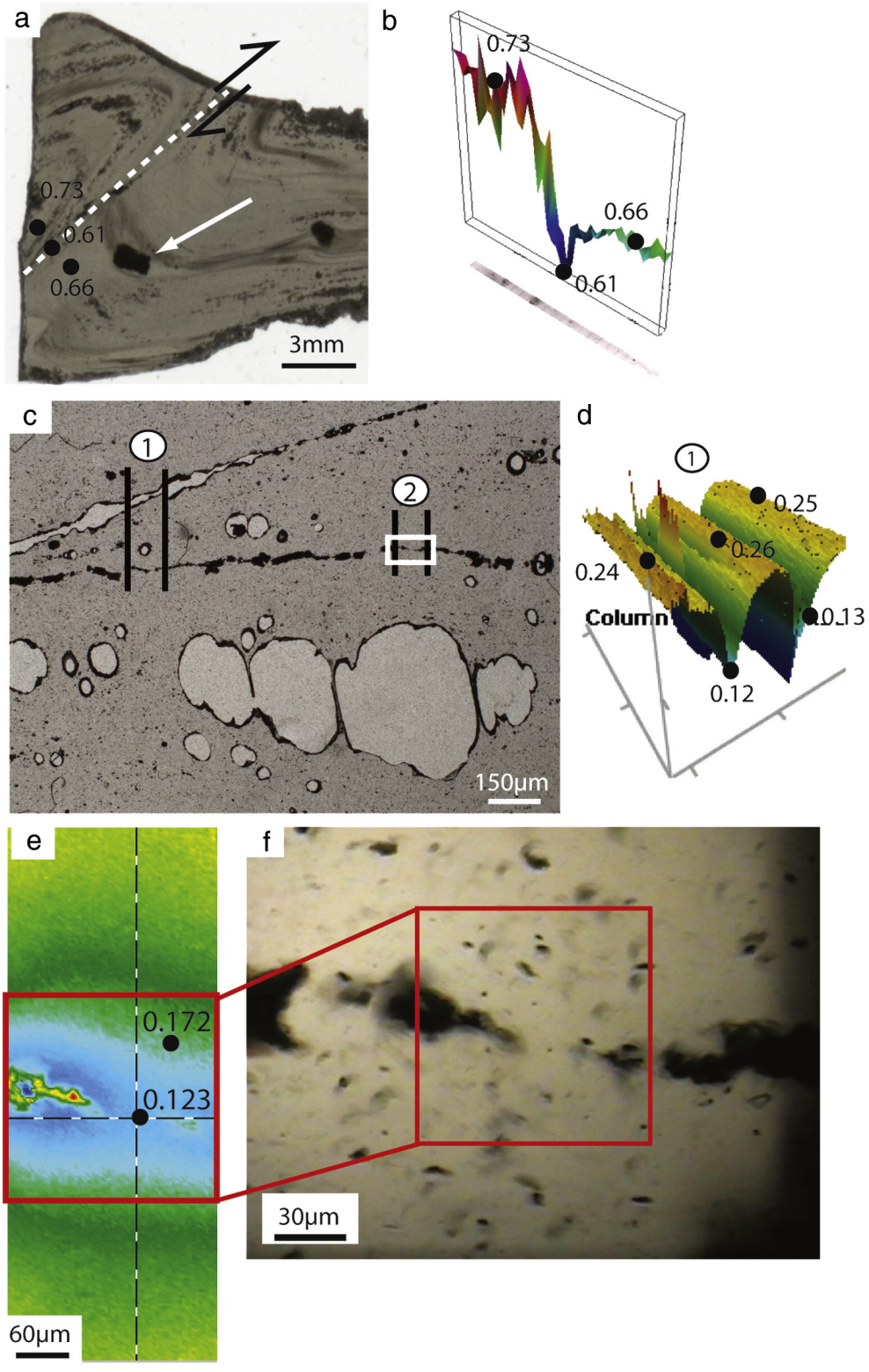

chemical signatures described here indicate that degassing due to fracturing is pervasive during silicic eruptions and has the potential to be a defusing mechanism for rhyolite volcanoes (e.g., Gonnermann and Manga, 2003).

A similar scenario to Cordón Caulle in Chile, may have occurred in the Monte Pilato-Rocche Rosse conduit, whereby non-explosive magma fragmentation develops branched fractures that intersect variably vesicular magma in the conduit and leads to efficient degassing (Schipper et al., 2013). In other words, in this case fracturing events will not only release water dissolved in melt but also have the potential to release gas trapped in bubbles, leading to vesicle collapse and forming tuffisites such as those documented above.

The evolution of rhyolitic eruptions from explosive to effusive may be summarized by focusing on the difference between the total volatile content of the magma, including H_2O in vesicles and dissolved in the melt (X_{tot}), and the H_2O content that the melt can dissolve at equilibrium (X_{eq}) for given P–T conditions. This can be considered a measure of the magma potential to erupt explosively ($W = X_{tot} - X_{eq}$). For a volume of melt that ascends and vesiculates, the total H_2O content will remain approximately constant if outgassing is inefficient, increasing its potential to decompress explosively (W increases). High-permeability fracturing events (e.g., Gonnermann and Manga, 2003) resulting from magma shearing against conduit walls or shock waves due to local pressure differences exceeding the threshold for fragmentation of vesicular melt, allow for a step-wise drop in that potential, and equilibration of the magma, decreasing explosivity (W decreases).

Extensive fracturing documented in Lipari samples, including the pervasive fragmentation in obsidian breccias and tuffisites (Figs. 5 and 6) and pumice breccias (Fig. 9), combined with development of H_2O-poor obsidian, suggest that fracture degassing may have played a significant role in defusing the intensity of the rhyolite eruption.

6. Conclusions

Monte Pilato-Rocche Rosse eruptions ejected rhyolite pyroclasts with relatively high and variable dissolved H_2O contents followed by

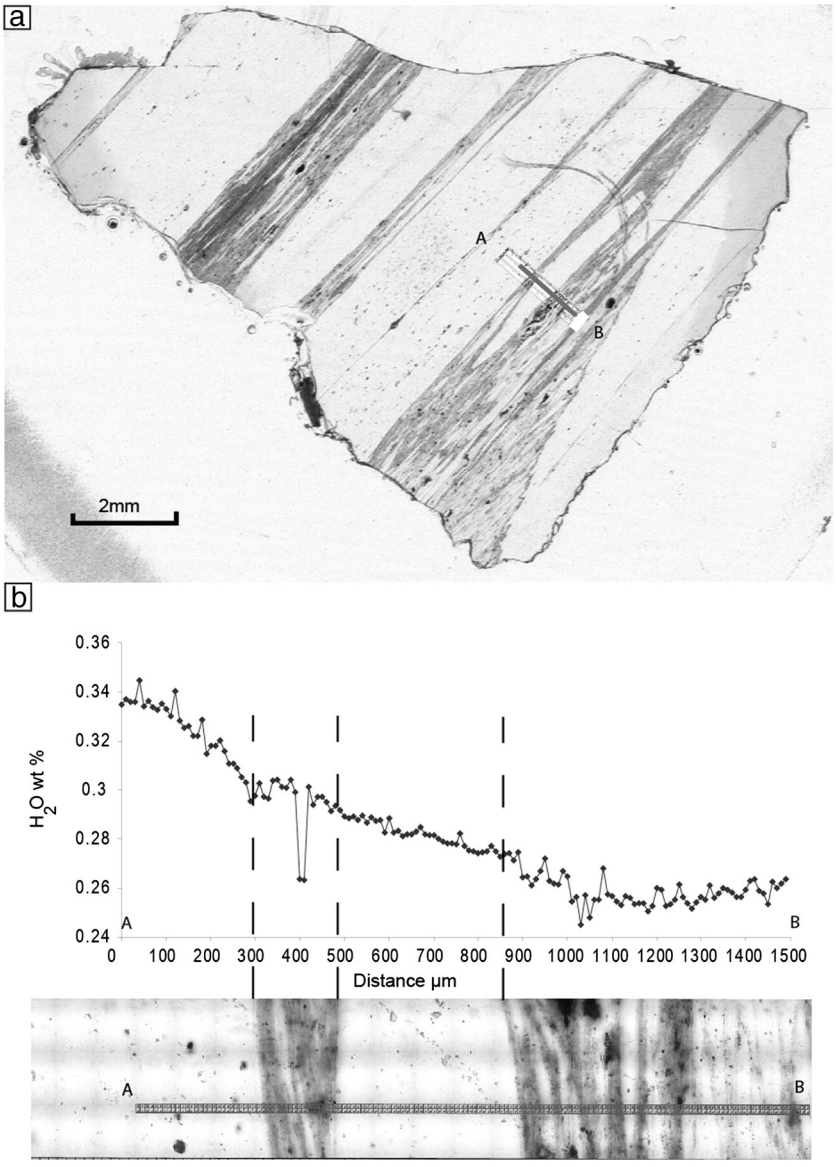

Fig. 11. H_2O variations in banded tuffisite obsidian from the Rocche Rosse pyroclasts: a) Wafer 92 μm thick from sample RRT. The rectangle highlights the area of two parallel synchrotron FTIR H_2O transects. Each transect (A to B) and measurement points along the transects are spaced at 10 μm. White is obsidian glass, grey is welded tuffisite. b) H_2O profile for transect A–B with calculated H_2O content values (average between the two parallel transects). H_2O content decreases gradually from A to B. The H_2O content in the clast-free obsidian band at A is ~0.08 wt.% higher than the clast-rich band near B. Standard deviation for H_2O content at each point is <0.002 wt.%. Dashed vertical lines separate boundaries between bands free of clastic material and bands rich in clasts.

effusion of H_2O-poor obsidian lava. During these eruptions, fracturing and healing of the high viscosity magmas is responsible for a number of different microstructures, ranging from simple planar faults, multiple cross-cutting fault sets, crenulated fault planes, and stretched out and complex obsidian and pumice breccias. These features indicate that fracturing was a common, repetitive and pervasive process in the conduit. This study also demonstrates that fracturing leads to diffusive H_2O loss from the melt, and that repeated fracturing events lead to high permeability gas loss events. Fractures not only capture newly exsolved volatiles, but also provide escape paths for volatiles trapped in vesicles. Thus, syn-eruptive degassing at depth through a combination of vesiculation and extensive fracturing could explain decreasing H_2O content from early explosive pyroclasts to late effusive lava flow. This process may be critical in defusing explosive potential of rhyolitic magmas.

Acknowledgements

This research forms part of AC's PhD thesis at Monash University. Valuable field work and early discussions were provided by Ray Cas, Guido Giordano, Arnaldo De Benedetti, Rossana De Rosa and Marcella Davì. We thank the Australian Synchrotron and Advanced Light Source for the beamtime required to perform this study and Ljiljana Puskar for her assistance during measurements. The authors thank Finley Shanks at the School of Chemistry for the help with FTIR measurements and Hugh Tuffen and Yan Lavallée for the constructive comments on an early version of the manuscript. We also acknowledge the constructive criticisms from Tina Neal and two anonymous reviewers.

Appendix A. Supplementary data

Supplementary data to this article can be found online at http://dx.doi.org/10.1016/j.jvolgeores.2014.12.014.

References

Barclay, J., Carroll, M.R., Houghton, B.F., Wilson, C.J.N., 1996. Pre-eruptive volatile content and degassing history of an evolving peralkaline volcano. J. Volcanol. Geotherm. Res. 74 (1–2), 75–87.

Blower, J., 2001. Factors controlling permeability–porosity relationships in magma. Bull. Volcanol. 63 (no. 7), 497–504.

Cabrera, A., Weinberg, R.F., Wright, H., Zlotnik, S., Cas, R.A.F., 2011. Melt fracturing and healing: a mechanism for degassing and origin of silicic obsidian. Geology 39, 67–70.

Caricchi, L., Pommier, A., Pistone, M., Castro, J., Burgisser, A., Perugini, D., 2011. Strain-induced magma degassing: insights from simple-shear experiments on bubble bearing melts. Bull. Volcanol. 73 (9), 1245–1257.

Castro, J.M., Dingwell, D.B., 2009. Rapid ascent of rhyolitic magma at Chaiten volcano, Chile. Nature 461 (7265), 780–783.

Castro, J.M., Manga, M., Martin, M.C., 2005. Vesiculation rates of obsidian domes inferred from H_2O concentration profiles. Geophys. Res. Lett. 32, 21307.

Castro, J.M., Beck, P., Tuffen, H., Nichols, A.R.L., Dingwell, D.B., Martin, M.C., 2008. Time-scales of spherulite crystallization in obsidian inferred from water concentration profiles. Am. Mineral. 93 (11–12), 1816–1822.

Castro, J., Burgisser, A., Schipper, C.I., Mancini, S., 2012a. Mechanisms of bubble coalescence in silicic magmas. Bull. Volcanol. 74 (10), 2339–2352.

Castro, J.M., Cordonnier, B., Tuffen, H., Tobin, M.J., Puskar, L., Martin, M.C., Bechtel, H.A., 2012b. The role of melt-fracture degassing in defusing explosive rhyolite eruptions at volcán Chaitén. Earth Planet. Sci. Lett. 333–334, 63–69.

Clay, P.L., O'Driscoll, B., Gertisser, R., Busemann, H., Sherlock, S.C., Kelley, S.P., 2012. Textural characterization, major and volatile element quantification and Ar–Ar systematics of spherulites in the Rocche Rosse obsidian flow, Lipari, Aeolian Islands: a temperature continuum growth model. Contrib. Mineral. Petrol. 1–23.

Cortese, M., Frazzetta, G., Lavolpe, L., 1986. Volcanic history of Lipari (Aeolian Islands, Italy) during the last 10,000 years. J. Volcanol. Geotherm. Res. 27 (no. 1-2), 117–133.

Davì, M., De Rosa, R., Barca, D., 2009. A LA-ICP-MS study of minerals in the Rocche Rosse magmatic enclaves: evidence of a mafic input triggering the latest silicic eruption of Lipari Island (Aeolian Arc, Italy). J. Volcanol. Geotherm. Res. 182 (no. 1-2), 45–56.

Davì, M., De Rosa, R., Holtz, F., 2010. Mafic enclaves in the rhyolitic products of Lipari historical eruptions; relationships with the coeval Vulcano magmas (Aeolian Islands, Italy). Bull. Volcanol. 72, 991–1008.

Davì, M., De Rosa, R., Donato, P., Sulpizio, R., 2011. The Lami pyroclastic succession (Lipari, Aeolian Islands): a clue for unravelling the eruptive dynamics of the Monte Pilato rhyolitic pumice cone. J. Volcanol. Geotherm. Res. 201 (no. 1-4), 285–300.

Dellino, P., La Volpe, L., 1995. Fragmentation versus transportation mechanisms in the pyroclastic sequence of Monte Pilato-Rocche Rosse (Lipari, Italy). J. Volcanol. Geotherm. Res. 64 (3–4), 211–231.

Dellino, P., La Volpe, L., 1996. Image processing analysis in reconstructing fragmentation and transportation mechanisms of pyroclastic deposits. The case of Monte Pilato-Rocche Rosse eruptions, Lipari (Aeolian islands, Italy). J. Volcanol. Geotherm. Res. 71 (1), 13–29.

Donato, P., Behrens, H., De Rosa, R., Holtz, F., Parat, F., 2006. Crystallization conditions in the Upper Pollara magma chamber, Salina Island, Southern Tyrrhenian Sea. Mineral. Petrol. 86 (1), 89–108.

Dunbar, N.W., Kyle, P.R., 1992. Volatile contents of obsidian clasts in tephra from the Taupo Volcanic Zone, New Zealand: implications to eruptive processes. J. Volcanol. Geotherm. Res. 49 (1–2), 127–145.

Eichelberger, J.C., Westrich, H.R., 1981. Magmatic volatiles in explosive rhyolitic eruptions. Geophys. Res. Lett. 8 (7), 757–760.

Eichelberger, J.C., Carrigan, C.R., Westrich, H.R., Price, R.H., 1986. Non-explosive silicic volcanism. Nature 323, 598–602.

Fink, J.H., 1980. Gravity instability in the Holocene Big and Little Glass Mountain rhyolitic obsidian flows, northern California. Tectonophysics 66 (1–3), 147–166.

Furukawa, K., Uno, K., Miyagi, I., 2010. Mechanisms of oxidation and degassing in the Takanoobane rhyolite lava of Aso Volcano, Japan. J. Volcanol. Geotherm. Res. 198 (3–4), 348–354.

Gamberi, F., Marani, M.P., 1997. Detailed bathymetric mapping of the eastern offshore slope of Lipari Island (Tyrrhenian Sea): insight into the dark side of an arc volcano. Mar. Geophys. Res. 19 (4), 363–377.

Gimeno, D., 2003. Devitrification of natural rhyolitic obsidian glasses: petrographic and microstructural study (SEM + EDS) of recent (Lipari island) and ancient (Sarrabus, SE Sardinia) samples. J. Non-Cryst. Solids 323 (1–3), 84–90.

Gioncada, A., Mazzuoli, R., Bisson, M., Pareschi, M.T., 2003. Petrology of volcanic products younger than 42 ka on the Lipari–Vulcano complex (Aeolian Islands, Italy): an example of volcanism controlled by tectonics. J. Volcanol. Geotherm. Res. 122 (3–4), 191–220.

Gonnermann, H.M., Manga, M., 2003. Explosive volcanism may not be an inevitable consequence of magma fragmentation. Nature 426 (6965), 432–435.

Gonnermann, H.M., Manga, M., 2005. Flow banding in obsidian: a record of evolving textural heterogeneity during magma deformation. Earth Planet. Sci. Lett. 236 (1–2), 135–147.

Gottsmann, J., Dingwell, D.B., 2001. The cooling of frontal flow ramps: a calorimetric study on the Rocche Rosse rhyolite flow, Lipari, Aeolian Islands, Italy. Terra Nova 13, 157–164.

Holland, A.S.P., Watson, I.M., Phillips, J.C., Caricchi, L., Dalton, M.P., 2011. Degassing processes during lava dome growth: insights from Santiaguito lava dome, Guatemala. J. Volcanol. Geotherm. Res. 202, 153–166.

Ihinger, P.D., Hervig, R.L., McMillan, P.F., 1994. Analytical methods for volatiles in glasses. Rev. Mineral. Geochem. 30, 67–121.

Jaupart, C., Allègre, C.J., 1991. Gas content, eruption rate and instabilities of eruption regime in silicic volcanoes. Earth Planet. Sci. Lett. 102 (3–4), 413–429.

Klug, C., Cashman, K.V., 1996. Permeability development in vesiculating magmas: implications for fragmentation. Bull. Volcanol. 58 (2), 87–100.

Lara, L.E., 2009. The 2008 eruption of the Chaiten Volcano, Chile: a preliminary report. Andean Geol. 36 (1), 125–129.

Lavallée, Y., Benson, P.M., Heap, M.J., Hess, K.-U., Flaws, A., Schillinger, B., Meredith, P.G., Dingwell, D.B., 2013. Reconstructing magma failure and the degassing network of dome-building eruptions. Geology 41 (4), 515–518.

Lowenstern, J.B., Bleick, H., Vazquez, J.A., Castro, J.M., Larson, P.B., 2012. Degassing of Cl, F, Li, and Be during extrusion and crystallization of the rhyolite dome at Volcan Chaiten, Chile during 2008 and 2009. Bull. Volcanol. 74 (10), 2303–2319.

Lucchi, F., Tranne, C.A., Rossi, P.L., 2010. Stratigraphic approach to geological mapping of the late Quaternary volcanic island of Lipari (Aeolian archipelago, southern Italy). Geol. Soc. Am. Spec. Pap. 464, 1–32.

Manley, C.R., Fink, J.H., 1987. Internal textures of rhyolites flows as revealed by research drilling. Geology 15, 549–552.

Mueller, S., Melnik, O., Spieler, O., Scheu, B., Dingwell, D.B., 2005. Permeability and degassing of dome lavas undergoing rapid decompression: an experimental determination. Bull. Volcanol. 67 (6), 526–538.

Newman, S., Stolper, E.M., Epstein, S., 1986. Measurement of water in rhyolitic glasses: calibration of an infrared spectroscopic technique. Am. Mineral. 71, 1521–1541.

Newman, S., Epstein, S., Stolper, E., 1988. Water, carbon dioxide, and hydrogen isotopes in glasses from the ca. 1340 A.D. eruption of the Mono Craters, California: constraints on degassing phenomena and initial volatile content. J. Volcanol. Geotherm. Res. 35 (1–2), 75–96.

Okumura, S., Nakamura, M., Takeuchi, S., Tsuchiyama, A., Nakano, T., Uesugi, K., 2009. Magma deformation may induce non-explosive volcanism via degassing through bubble networks. Earth Planet. Sci. Lett. 281 (3–4), 267–274.

Okumura, S., Nakamura, M., Nakano, T., Uesugi, K., Tsuchiyama, A., 2010. Shear deformation experiments on vesicular rhyolite: implications for brittle fracturing, degassing, and compaction of magmas in volcanic conduits. J. Geophys. Res. 115 (no. B6), B06201.

Okumura, S., Nakamura, M., Uesugi, K., Nakano, T., Fujioka, T., 2013. Coupled effect of magma degassing and rheology on silicic volcanism. Earth Planet. Sci. Lett. 362, 163–170.

Pallister, J.S., Diefenbach, A.K., Burton, W.C., Munoz, J., Griswold, J.P., Lara, L.E., Lowenstern, J.B., Valenzuela, C.E., 2013. The Chaiten rhyolite lava dome: eruption sequence, lava dome volumes, rapid effusion rates and source of the rhyolite magma. Andean Geol. 40 (2), 277–294.

Rust, A.C., Cashman, K.V., 2004. Permeability of vesicular silicic magma: inertial and hysteresis effects. Earth Planet. Sci. Lett. 228 (1–2), 93–107.

Rust, A., Cashman, K., 2007. Multiple origins of obsidian pyroclasts and implications for changes in the dynamics of the 1300 B.P. eruption of Newberry Volcano, USA. Bull. Volcanol. 69, 825–845.
Rust, A.C., Cashman, K.V., 2011. Permeability controls on expansion and size distributions of pyroclasts. J. Geophys. Res. 116, B11202. http://dx.doi.org/10.1029/2011JB008494.
Rust, A.C., Cashman, K.V., Wallace, P.J., 2004. Magma degassing buffered by vapor flow through brecciated conduit margins. Geology 32 (4), 349–352.
Saar, M.O., Manga, M., 1999. Permeability–porosity relationship in vesicular basalts. Geophys. Res. Lett. 26 (1), 111–114.
Schipper, C.I., Castro, J.M., Tuffen, H., James, M.R., How, P., 2013. Shallow vent architecture during hybrid explosive–effusive activity at Cordón Caulle (Chile, 2011–12): evidence from direct observations and pyroclast textures. J. Volcanol. Geotherm. Res. 262, 25–37.
Shea, T., Gurioli, L., Houghton, B.F., 2012. Transitions between fall phases and pyroclastic density currents during the AD 79 eruption at Vesuvius: building a transient conduit model from the textural and volatile record. Bull. Volcanol. 74, 2363–2381.
Sparks, R.S.J., 2003. Dynamics of magma degassing. Geol. Soc. Lond., Spec. Publ. 213 (1), 5–22.
Spieler, O., Kennedy, B., Kueppers, U., Dingwell, D.B., Scheu, B., Taddeucci, J., 2004. The fragmentation threshold of pyroclastic rocks. Earth Planet. Sci. Lett. 226, 139–148.
Stasiuk, M.V., Barclay, J., Carroll, M.R., Jaupart, C., Ratté, J.C., Sparks, R.S.J., Tait, S.R., 1996. Degassing during magma ascent in the Mule Creek vent (USA). Bull. Volcanol. 58 (2), 117–130.
Stevenson, R.J., Briggs, R.M., Hooder, A.P.W., 1994. Physical volcanology and emplacement history of the Ben-Lomond rhyolite lava flow, Taupo volcanic center, New Zealand. J. Geol. Geophys. 37, 345–358.
Takeuchi, S., Nakashima, S., Tomiya, A., 2008. Permeability measurements of natural and experimental volcanic materials with a simple permeameter: toward an understanding of magmatic degassing processes. J. Volcanol. Geotherm. Res. 177 (2), 329–339.
Tranne, C.A., Lucchi, F., Calanchi, N., Lanzafame, G., Rossi, P.L., 2002. Geological map of the island of Lipari (Aeolian Islands). Università di Bologna e INGV, L.A.C. Firenze.
Tuffen, H., Castro, J.M., 2009. The emplacement of an obsidian dyke through thin ice: Hrafntinnuhryggur, Krafla Iceland. J. Volcanol. Geotherm. Res. 185 (4), 352–366.
Tuffen, H., Dingwell, D., 2005. Fault textures in volcanic conduits: evidence for seismic trigger mechanisms during silicic eruptions. Bull. Volcanol. 67 (4), 370–387.
Tuffen, H., Dingwell, D.B., Pinkerton, H., 2003. Repeated fracture and healing of silicic magma generate flow banding and earthquakes? Geology 31 (12), 1089–1092.
Tuffen, H., Owen, J., Denton, J., 2010. Magma degassing during subglacial eruptions and its use to reconstruct palaeo-ice thicknesses. Earth Sci. Rev. 99, 1–18.
Villemant, B., Boudon, G., 1998. Transition from dome-forming to plinian eruptive styles controlled by H_2O and Cl degassing. Nature 392 (6671), 65–69.
Von Aulock, F.W., Nichols, A.R.L., Kennedy, B., Oze, C., 2013. Timescales of texture development in a cooling lava dome. Geochim. Cosmochim. Acta 114, 72–80.
Watkins, J.M., Manga, M., DePaolo, D.J., 2012. Bubble geobarometry: a record of pressure changes, degassing, and regassing at Mono Craters, California. Geology 40 (8), 699–702.
Watt, S.F.L., Pyle, D.M., Mather, T.A., 2013. Evidence of mid-to late-Holocene explosive rhyolitic eruptions from Chaiten Volcano, Chile. Andean Geol. 40 (2), 216–226.
Weaire, D., 2008. The rheology of foam. Curr. Opin. Colloid Interface Sci. 13 (3), 171–176.
Westrich, H.R., Stockman, H.W., Eichelberger, J.C., 1988. Degassing of rhyolitic magma during ascent and emplacement. J. Geophys. Res. 93, 6503–6511.
Wright, H.M.N., Weinberg, R.F., 2009. Strain localization in vesicular magma: implications for rheology and fragmentation. Geology 37, 1023–1026.
Wright, H.M.N., Roberts, J.J., Cashman, K.V., 2006. Permeability of anisotropic tube pumice: model calculations and measurements. Geophys. Res. Lett. 33 (no. 17), L17316.
Yoshimura, S., Nakamura, M., 2008. Diffusive dehydration and bubble resorption during open-system degassing of rhyolitic melts. J. Volcanol. Geotherm. Res. 178 (1), 72–80.
Yoshimura, S., Nakamura, M., 2010. Fracture healing in a magma: an experimental approach and implications for volcanic seismicity and degassing. J. Geophys. Res. Solid Earth 115, B09209. http://dx.doi.org/10.1029/2009JB000834.
Zhang, Y., Jenkins, J., Xu, Z., 1997. Kinetics of the reaction $H_2O + O - 2OH$ in rhyolitic glasses upon cooling: geospeedometry and comparison with glass transition. Geochim. Cosmochim. Acta 61, 2167–2173.